Geophysical Research Letters

Supporting Information for

Aeolian Changes at the InSight Landing Site on Mars: Multi-instrument Observations

Charalambous C.[1], McClean J. B.[1], Baker M.[2], Pike W. T.[1], Golombek M.[3], Lemmon M.[4], Ansan V.[5], Perrin C.[6], Spiga A.[7,8], Lorenz R.[9], Banks M. E.[10], Rodriguez S.[6], Murdoch N.[11], Weitz C. M.[12], Daubar I. J.[13], Grant J. A.[14], Warner N. H.[15], Hauber E.[16], Stott A. E.[1], Johnson C. L.[17,18], Mittelholz A.[17], Warren T.[19], Navarro S.[20], Sotomayor L. M.[20], Maki J.[3], Lucas A.[6], Banfield D.[21], Newman C.[22], Viúdez-Moreiras D.[20], Pla-García J.[20], Lognonné P.[6], Banerdt W. B.[3]

[1]Imperial College London, *Department of Electrical and Electronic Engineering, South Kensington Campus, Exhibition Road, SW7 2AZ, United Kingdom*

[2]Johns Hopkins University, *Morton K. Blaustein Department of Earth and Planetary Sciences, 301 Olin Hall, 3400 N. Charles St, Baltimore, MD 21218, USA*

[3]Jet Propulsion Laboratory, California Institute of Technology, *Pasadena, CA 91109, USA*

[4]Space Science Institute, *Boulder, CO, USA*

[5]Laboratoire de Planétologie et Géodynamique, UMR6112-CNRS, Univ. Nantes, *2 rue de la Houssinière, BP 92208, 44322 Nantes Cedex 3, France*

[6]Université de Paris, Institut de physique du globe de Paris, CNRS, *F-75005 Paris, France*

[7]Laboratoire de Météorologie Dynamique / Institut Pierre-Simon Laplace (LMD/IPSL), Sorbonne Université, Centre National de la Recherche Scientifique (CNRS), École Polytechnique,École Normale´ Supérieure (ENS), *Campus Pierre et Marie Curie BC99, 4 place Jussieu 75005 Paris, France*

[8]Institut Universitaire de France, *1 rue Descartes, Paris, France*

[9]Johns Hopkins Applied Physics Laboratory, *11100 Johns Hopkins Road, Laurel, MD 20723, USA*

[10]NASA Goddard Space Flight Center, *8800 Greenbelt Road, Greenbelt, MD 20771, USA*

[11]Institut Supérieur de l'Aéronautique et de l'Espace (ISAE-SUPAERO), *10 Avenue Edouard Belin, 31400 Toulouse, France*

[12]Planetary Science Institute, *1700 E Fort Lowell, Suite 106, Tucson, AZ 85719, USA*

[13]Brown University, Department of Earth, Environmental, and Planetary Sciences, *Campus Box 1846, Providence, RI 02912-1846, USA*

[14]Smithsonian Institution, *Center for Earth and Planetary Studies, National Air and Space Museum, 600 Independence Ave. SW, Washington, DC 20560, USA*

[15]State University of New York at Geneseo, Department of Geological Sciences, *1 College Circle, Geneseo, NY 14454, USA*

[16] German Aerospace Center, Institute of Planetary Research, *Rutherfordstr. 2, 12489 Berlin, Germany*

[17]University of British Columbia, *Department of Earth, Ocean and Atmospheric Sciences, Vancouver, BC, V6T 1Z4, Canada*

[18]Planetary Science Institute, 1700 East Fort Lowell, *Suite 106, Tucson, AZ 85719 USA*

[19]University of Oxford, *University of Oxford, Department of Physics, Parks Road, Oxford OX1 3PU, UK*

[20]Centro de Astrobiologíaa (CSIC-INTA), *Torrejón de Ardoz, Madrid, Spain*

[21]Cornell University, *Cornell Center for Astrophysics and Planetary Science, Ithaca, NY, 14853, USA*

[22]Aeolis Research, *333 N Dobson Road, Unit 5, Chandler AZ 85224-4412, USA*

Contents of this file

Text S1 to S19

Figures S1 to S19

Tables S1 to S3

Additional Supporting Information (Files uploaded separately)

Movie S1: Sol 10-106 West lander footpad change detection IDC movie

Movie S2: Sol 18-20 1st Change of west lander footpad change detection ICC movie

Movie S3: Sol 26/noon-26/afternoon 2nd Change of west lander footpad change detection ICC movie

Movie S4: Sol 65-66 3rd Change of west lander footpad change detection ICC movie

Movie S5: Sol 4-66 ICC lens gradual dust particle cleaning movie

Movie S6: Sol 232-239 Localized dust removal on tether appearing as a dark spot ICC movie

Movie S7: Sol 234-257 Localized dust removal on tether appearing as a dark spot IDC movie

Movie S8: Sol 65 13:25-14:30 Dust aggregate motion on the Wind and Thermal Shield and solar panel small cleaning IDC movie

Movie S9: Sol 63-65 13:25-14:30 Small cleaning even on solar panel appearing as a dark streak IDC movie

Movie S10: Sol 362-364 Surface creep of 2 mm granules IDC movie

Movie S11: Sol 362-364 Zoom-in on the train of 2 mm granules surface creeping IDC movie

Movie S12: Sol 383-385 Surface creep, dust-coating removal, saltation, mini-pile collapse IDC movie

Movie S13: Sol 383-385 Surface creep of a granule 3 mm in diameter displacing 4 mm IDC movie

Movie S14: Sol 383-385 Surface creep of a granule 2.55 mm in diameter displacing 21 mm IDC movie

Movie S15: Sol 383-385 Mini pile collapsing IDC movie

Movie S16: Sol 385-386 Dust-coating removal from rock surfaces IDC movie

Movie S17: Sol 228-232 Visible surface dark streak from a ‘feathered’ dust devil track, with illustration of image differencing ICC movie

Introduction

This supplementary information section provides the necessary material for the better understanding of the aeolian changes identified at the InSight landing site on Mars. The data and lander instruments are addressed in S1-2. All the multi-instrument data were retrieved for each period between which an aeolian change was identified in the before and after images, investigated over a total of 400 sol of operations. For each time-lapsed period, the candidate vortex and wind peak were chosen to be the maximum in this period. For Sol 385, the particular selection of vortex was validated via atmospheric and seismic modelling.

The procedure of identifying aeolian changes is described in S3-6. A detailed description of the conditions, multi-instrument measurements and grain-size measurements for the most prominent aeolian changes are described in S7-13. The supplementary information pays special tribute to the Sol 385 event: 1) it details multiple grain measurements that were identified as moving, 2) atmospheric and seismic modelling, 3) HiRISE orbital image differencing showing the same dust devil track as observed on the surface from lander cameras and 4) analyses the phenomenon of missing wind data points during the passage of vortex, due to high vorticity conditions for reliable wind retrieval. The final section of the supplementary information looks into the fluid threshold models, how the aerodynamic surface roughness length could possibly vary substantially at the landing site and finally, an investigation on the origin of the dark spots appearing in the FOV of the ICC camera is included.

A catalogue of the changes observed, the before-and-after images when these are identified, along with the maximum wind and pressure drop during the time-lapsed period is included below in Table SI1.

LMST 1 (ICC/IDC taken at)	LMST 2 (ICC/IDC taken at)	sol1	sol2	Comments	wind speed max	wind direction of max speed	sol of wind max	pressure max	sol of max pressure
13:37:57	13:02:32	18	20	ICC cleaning + DD track + major footpad change	23.6	280	19	5.8	19
17:46:08	18:01:06	20	22	ICC cleaning	-	-	-	-	-
14:11:29	13:03:34	23	24	ICC cleaning + small footpad change	25.9	310	24	3.7	24
15:39:42	15:52:58	25	26	ICC major cleaning	28.2	280	26	4	26
11:02:53	15:52:58	26	26	ICC cleaning + major footpad change	28.2	280	26	4	26
15:52:58	18:35:08	26	30	ICC minor cleaning	23	266	29	3.7	29
12:32:39	12:47:24	37	37	ICC cleaning same sol	None	None	None	None	None
12:47:24	13:23:52	37	37	ICC cleaning same sol	None	None	None	None	None
16:45:50	14:28:24	38	39	ICC major cleaning	24.8	280	39	5.7	39
17:27:12	18:05:26	42	44	ICC major cleaning	18.8	135	44	2.9	44
18:05:26	18:08:08	44	46	ICC biggest cleaning	25.91	130	46	1.9	46
18:08:08	17:07:14	46	48	ICC cleaning	17.3	130	48	0.8	47
17:07:14	17:25:45	48	50	ICC cleaning	16.6	100	49	2.8	49
13:43:06	13:48:20	63	65	ICC cleaning	15.1	1	64	4.1	65
13:25:54	14:30:48	65	65	IDC same sol Solar array cleaning, WTS particles	20.1	170	65	9.2	65
13:48:20	10:05:00	65	66	ICC major cleaning, major footpad	20.1	170	65	9.2	65
16:40:39	16:40:39	164	166	ICC cleaning + DD track	17.1	155	165	4.1	166
16:40:39	16:19:33	166	167	DD track	18.8	135	167	3	167
16:19:33	16:17:08	167	168	ICC surface dark spot	14.7	170	168	3.5	168
16:30:40	16:30:40	179	180	DD track	16.16	135	180	2.3	180
17:22:36	16:41:29	201	202	DD track	19.5	145	202	1.19	202
13:46:26	13:26:16	203	205	DD disturbance - track geometrically overlaps to sol 202 track	18.9	160	204	2.1	204
17:31:16	13:17:55	230	232	ICC minor cleaning + Feathered DD track + Surface dark spot	19.3	130	231	6.8	231
08:01:03	15:42:49	235	235	Dark spots on tether (dust removal)	17.2	130	235	1.6	235
16:32:54	13:10:57	258	259	DD track	22.4	155	258	2.2	257
13:10:57	15:31	259	261	DD track	22	130	261	2.29	261
15:53:49	15:53:49	362	364	IDC mm-sized clast motion + subtle changes	31.6	130	364	3.5	364
11:55:58	15:53:49	385	385	IDC mm-sized clast motion +saltation+dust lift-off+ICC DD track	30.5	95	385	5.5	385

Table SI1: Catalogue of the most prominent aeolian changes observed during the first 400 sols of operations at InSight. The catalogue includes the associated max wind speed and direction, and max pressure drop that was recorded during the time interval of the before and after images when the aeolian change occured.

SI.1 Auxiliary Payload Sensor Suite

a. Wind and pressure data

The Temperature and Wind for InSight (TWINS) sensor booms employ hot-wire anemometry, based on Curiosity's Rover Environmental Monitoring Station (REMS). The booms are located by the edge of InSight's deck and face outward over InSight's west and east solar panels at approximately 1.2 m from the surface. More specifically, we use the a local coordinate system, the InSight local lander level (LL) in which the Y+ boom faces to the east with the Y- to the west (X+ is in the North, see Fig 2e for the lander schematic). Due to the lander's tilt within Homestead hollow, they stand at slightly different heights of less than 10 cm difference (Banfield, Spiga et al. 2020). Data are continuously recorded at 1 Hz (wind) and 20 Hz (pressure), with wind and pressure data transmitted at 0.1 Hz / 2 Hz (1 Hz / 10 Hz after sol ~165). Downlink requests for specific events of interest allow small time-windows of pressure data to be transmitted at 20 Hz. There is an accuracy of 1 ms^{-1} for wind speed, 22.5° for wind direction, and 5 K for temperature (Banfield, Spiga et al., 2020). The wind speed and direction are obtained after reconstruction from the Y+ and Y- boom measurements. This takes into account the position of each boom compared to the prevailing wind, and further corrections based on simulations by computational fluid dynamics allow for the degree of interaction from the lander elements in retrieving wind measurements.

The two booms only capture average winds at different peak speeds during the fast rotations in the encounter of a passing vortex. This is due to the high perturbations and increased turbulence at the closest encounter of a passing vortex, making wind retrieval challenging. One boom may therefore better capture the wind speed at any given moment - and which boom best captures the wind speed might vary on short timescales during vortex encounters. We therefore use the maximum of the two booms during all vortex encounters, consistently throughout the paper.

a. Magnetic data

Throughout the paper, the magnetic field components, N (northward), E (eastward), and Z (downward) follow the local lander level, which is InSight's local coordinate system, consistent with the frame used for the TWINS. Data are continuously recorded at sampling rates of 20 Hz, transmitted at 0.2 Hz up to sol 183. The sampling rate was increased to 2 Hz on sol 183, dropping back down to 0.2 Hz on sol 261 followed by a data gap due to the solar conjunction. After solar conjunction (from sol 284 onwards) the data downlink was resumed with 2 Hz data. Downlink requests for specific events of interest allow small time-windows to be transmitted at 20 Hz. We use the continuous data in this study.

SI.2 InSight Cameras

The Instrument Context Camera (ICC) is mounted on the lander body underneath the top deck and has a "fisheye" field of view 120 degrees wide of the workspace in the south to southwest of the lander, including the lander's west footpad, the umbilical tether connecting SEIS and the lander, the HP3 and SEIS itself (Suppl.Fig.1). The Instrument Deployment Camera (IDC) is mounted at the elbow of the robotic arm which allows for a panoramic view of the terrain surrounding the landing site, but also parts of the lander itself such as the footpads or the deck. Typical ground standoff distances capture images at 1 mm/pixel (Maki et al. 2018), while the resolution of the IDC when the arm's scoop is pinned onto the surface overlooking the HP3 can achieve the closest height to the surface, at 0.53 mm/pixel from a 0.65 cm height.

SI.3 Imaging and aeolian change experiment campaigns

Imaging of the workspace with the IDC was more frequent in the early mission, while the IDC was not occupied by HP3 recovery activities. The robotic arm has since been unavailable to image surroundings for changes. Current InSight imaging data is downlinked at a daily cadence with ICC imaging as an aeolian change detection experiment aimed at detecting coarse changes in the FOV. Specific IDC imaging that allows for aeolian change observation while the Instrument Deployment Arm (IDA) overlooks the HP3 mole has been taken at least once per sol, from Sol 374 onward, under a different change detection experiment aimed at finer motion on the surface. This particular configuration brings the IDC camera to a position nearest to the surface, which also allows us to qualitatively observe, but not resolve, sub-mm motion.

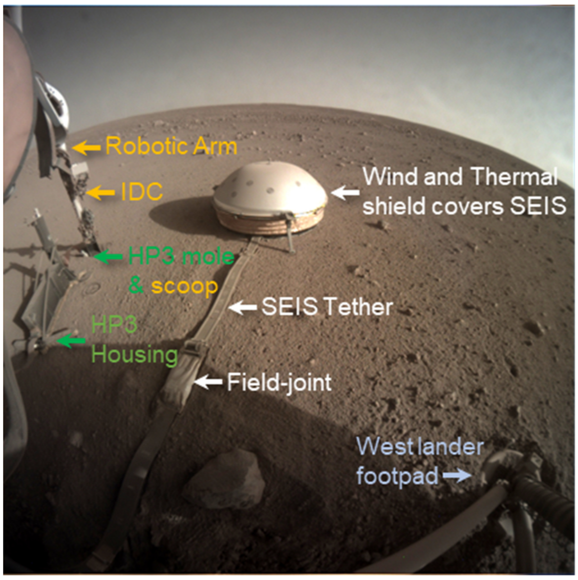

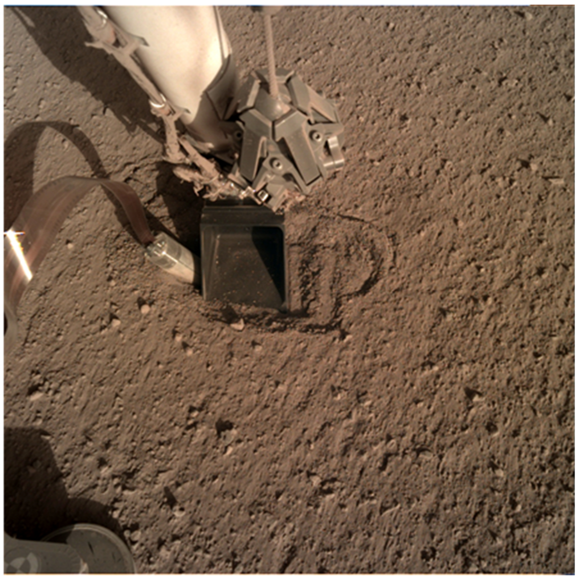

Figure SI1 (left) ICC image on S385 indicating the lander and instrument components (right) IDC image from S385, demonstrating the closest position to the surface the camera has achieved, at a 0.65 m height.

SI.4 Image search

The image search included images taken both for specific aeolian change detection campaigns, but also daily images for engineering purposes. It is noted that most aeolian changes were detected in images prior to any set campaign experiments. These identified changes have provided invaluable knowledge for setting up subsequent change detection campaigns. ICC image campaigns have allowed for a multitude of DD tracks to be identified through image differencing, while IDC campaigns permitted changes such as mm-sized granule creep to be observed, and dust lifting to be confirmed.

SI.5 Image comparison procedure

Generally, to identify changes, images under the same illumination conditions are compared. Because this is not always possible, images with different illuminations can provide some evidence of modification but an after-image is required to be captured with similar sun elevation to validate any changes. Cross-checking between IDC and ICC is sometimes sufficient to validate a change that emerged under different When a change is observed, APSS and SEIS data is analysed over the period between the acquisition of the two images. In addition, robotic arm activity is taken into consideration - for example to avoid falsely identifying particles falling off the arm during its motion as due to aeolian effects.

SI.6 Image differencing

We define the image difference of two images as the single-passed absolute difference of intensity value at each pixel. Two images are compared as pixel arrays, where we assume the first image I_{t-T} is the background array we attempt to remove at time $t-T$, where T defines the temporal distance. The difference of the two pixel-array values is defined as:

$$D(i, j) = I_{t-T}(i, j) - I_t(i, j) \qquad (1)$$

where i is the i-th row and j the j-th column in the pixel array from a total number of pixels M that must be equal in the two arrays I_{t-T} and I_T, hence the resolution. Image difference was implemented in MATLAB. Direct differencing can be noisy due to high sensitivity to lighting and motion, therefore binning, via a two-dimensional median filtering of an $n \times n$ pixel kernel (usually 2 x 2) is applied to reduce noise and graininess, and to improve sub-pixel misalignments. Further image enhancement techniques are applied such as contrast stretching, histogram equalization and adaptive histogram equalization.

Aligned pixels and similar illumination conditions allow for image differencing. Due to the IDA being easily vibrated from wind gusts and thus shifting in pixel location, in contrast to the ICC which is fixed in position, IDC image differencing becomes more challenging as the process is very sensitive to pixel location shifts resulting in image degradation. In such occasions, image registration is required which is done manually, as best as possible. During the more recent part of the mission, the robotic arm configuration had the scoop pressing over the HP3 mole, providing an excellent opportunity to maintain a steady position and thus allowing for excellent IDC differencing under similar photometric conditions.

Finally, grayscale thresholding was applied on several occasions. Thresholding allows the changes to emerge as white pixels, which can then be merged as an overlaid layer onto the raw images, highlighting changes and allowing for better visualisation to a reader not familiar with the reference background.

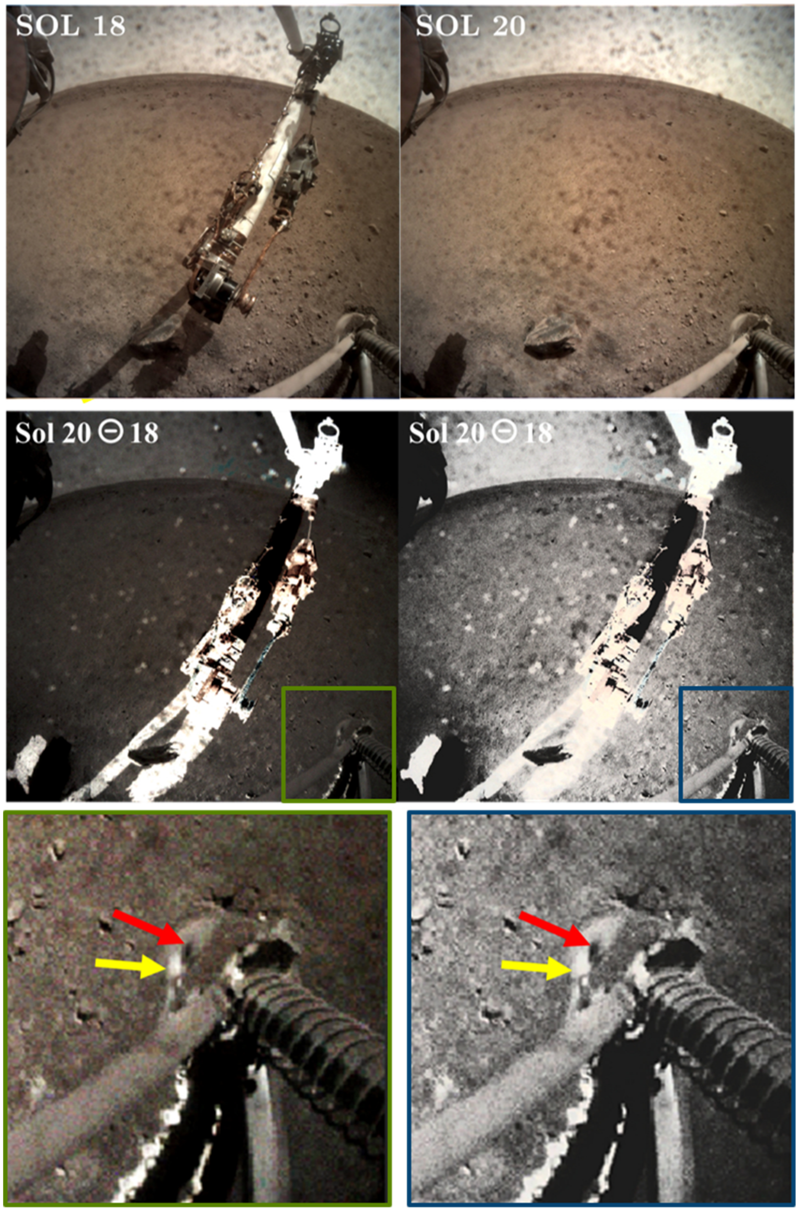

Figure SI2: (Top row) Sol 18 vs Sol 20 raw images. Notice that due to the bright reflection of the white part of the arm, the overall image illumination is lower (Middle row) Difference of Sol 18 vs Sol 20 images, shown with two difference contrast adjustment techniques. Image adjustment of intensity values based on the subtraction values is shown on the left and a histogram equalization on the right. The disappearance of the arm is evident, with the strongly illuminated part appearing bright, and the darkly illuminated part of the arm appearing as a dark difference (negative result, therefore set at a zero intensity value), because this is relative to the background assumption. The removal of dust on the lens is strongly visible; these appear as bright spots, since the visibility on Sol 20 has been increased. (Bottom row) Zoomed-in view of the footpad from the differencing in middle row. The footpad shows the removal of a patch of dust as a bright difference due to the footpad becoming brighter (yellow arrow) and displacement of some of the dusty material to the upper part of the patch (red arrow) showing up as a darker spot in the differencing due to new material covering a previously unoccupied area of the footpad.

SI.7 West Lander footpad and WTS measurements

Measurements for the grains that *did not* move on the footpad (which allows one to constrain the size-range for motion based on Shao and Lu's (2000) model, are shown in Fig. SI3 and Table SI2.

Measurements for the “flaky” appearing, dust-aggregate sizes that *did* move on the WTS are shown in Fig. SI3 and Table SI2.

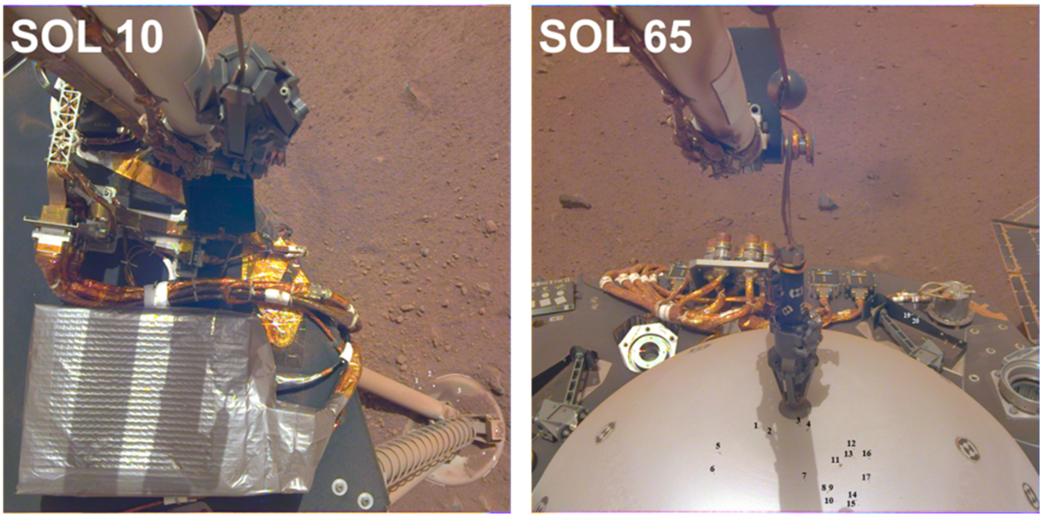

Figure SI3: The numbered grains are measured and listed in the supplementary spreadsheet for the IDC images: (left) on the footpad for sol 10 and (right) on the Wind and Thermal Shield for sol 65.

Sol 10_106 grain displacement on west footpad

image 1 D001L0010_597413235CPG_F0002_0080M2_11h19_01

image 2 D001L0106_605946913CPG_F0002_0080M2_14h20_22

#grain WTS	width (px)	length (px)	diameter (px)	accuracy (px)	diameter (mm)	accuracy (mm)
1	5	3	3.87	1.40	5.03	1.82
2	4	4	4.00	1.40	5.20	1.82
3	3	2	2.45	1.40	3.18	1.82
4	3	3	3.00	1.40	3.90	1.82

Table SI2: Measurements for the grains that *did not* move on the footpad in Figure SI3. This allows one to constrain the size-range for motion based on Shao and Lu’s (2000) model (see Fig. 4c in main text)

Sol 65 grain displacement on WTS

image 1 D000M0065_602301091CPG_F0000_12h35_05

image 2 D000M0065_602305092CPG_F0000_13h39_59

#grain WTS	width (px)	length (px)	diameter (px)	accuracy (px)	diameter (mm)	accuracy (mm)
1	2	4	2.83	1.4	2.26	1.12
2	2	7	3.74	1.4	2.99	1.12
3	3	5	3.87	1.4	3.10	1.12
4	4.25	8.5	6.01	1.4	4.81	1.12
5	3	8.6	5.08	1.4	4.06	1.12
6	1.5	2	1.73	1.4	1.39	1.12
7	1.5	1.5	1.50	1.4	1.20	1.12
8	2.8	3.6	3.17	1.4	2.54	1.12
9	1.5	1.5	1.50	1.4	1.20	1.12
10	2.85	2.85	2.85	1.4	2.28	1.12
11	6.4	7.82	7.07	1.4	5.66	1.12
12	2.85	4.24	3.48	1.4	2.78	1.12
13	2.85	3.6	3.20	1.4	2.56	1.12
14	2.85	3.6	3.20	1.4	2.56	1.12
15	2.85	2.85	2.85	1.4	2.28	1.12
16	2.85	3.6	3.20	1.4	2.56	1.12
17	2.85	2.85	2.85	1.4	2.28	1.12
#grain deck	width (px)	length (px)	diameter(px)	accuracy (px)	diameter (mm)	accuracy (mm)
18	2.82	2.82	2.82	1.4	2.26	1.12
19	3.6	3.6	3.60	1.4	2.88	1.12
20	4.25	4.25	4.25	1.4	3.40	1.12

Table SI3: Measurements for the “flaky” appearance, dust-aggregates that moved or disappeared on the wind and thermal shield on sol 65

SI.8 Sol 18-20

The first aeolian change event was detected between ICC images taken late-afternoon on sol 18 at 17:00 LMST, and sol 20 at 13:02 LMST. Two distinct changes were observed on the west footpad: a partial area was removed from the original dust patch while a new streak of dust appeared, oriented approximately north-south (see differencing in Fig. S1)). The differencing of the footpad images over sols 18 and 20 shown in Fig. S1 reveals one brighter and one darker area. These areas suggest that while some of the dusty patch was lifted off, part of it was redeposited or transported further up along the footpad. For a $z_0 \approx 5$ *mm*, the wind speed exceeded the fluid threshold twice in this period, with peak wind speeds of 21.8 ms^{-1} at 2018-12-16 08:13 UTC and 23.6 ms^{-1} at 2018-12-16 08:19 UTC. The first peak was associated with a 0.3 Pa pressure drop, and the second peak was associated with a 1.7 Pa pressure drop. There were three other notable pressure drops with a magnitude larger than these two: 2.1 Pa at 2018-12-16 04:44 UTC, 4.8 Pa, 17.32 ms^{-1} at 2018-12-16 08:36 UTC, and 5.8 Pa, 20.7 ms^{-1} at 2018-12-16 09:02 UTC. The latter is the best candidate vortex, also exhibiting a correlation with a magnetic signature (Fig. SI3).

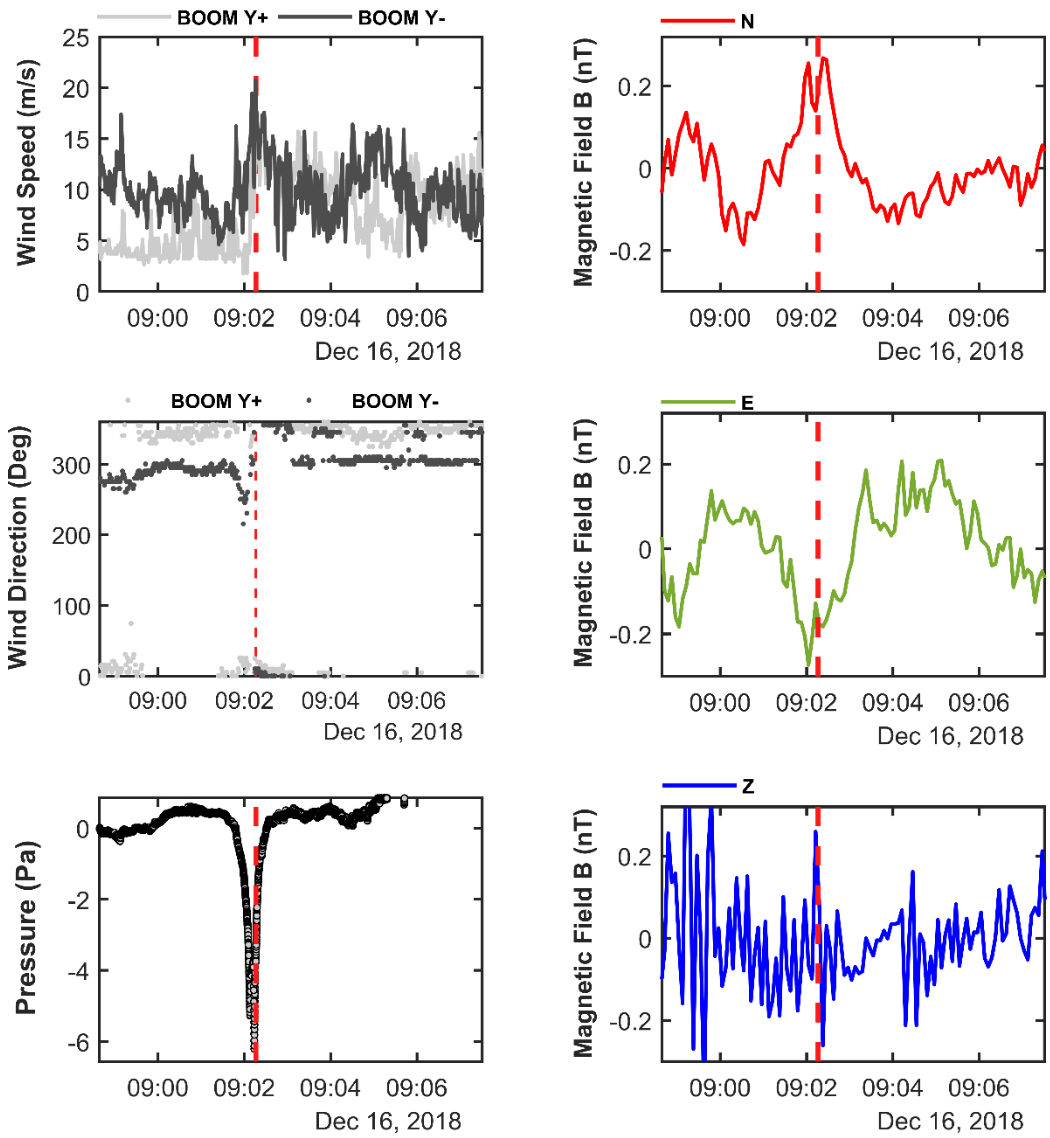

Figure SI4: The candidate meteorological event on sol 19 that has most likely caused the aeolian changes seen on the footpad, ICC lens cleaning and a DD track changes. Evidence of close passage by the lander is evident, along with the first DD track observed in differenced ICC images (Time axis in UTC).

SI.9 Sol 26

The partial removal of the dust patch was associated with the footpad brightening in appearance. The streak of dust first appearing on sol 20 increased, becoming more ellipsoidal with a north-south major axis and darker in colour. Two wind peaks were observed in the time-lapsed period of ICC images between 11:02-15:52 LMST as shown in Fig.SI5; the first peak was associated with a 2.9Pa pressure drop, and the second peak was associated with a 4.1 Pa pressure drop. The latter's data with the maximum wind peak is shown in Fig.SI5a, with an evident excursion in the magnetic field at the time of the vortex's passage. For a $z_0 \approx 5$ *mm*, the wind speed exceeded the fluid threshold twice for detaching particles of 100 microns, with a peak wind speed of 28.2ms^{-1} at 2018-12-23 13:19:49 UTC.

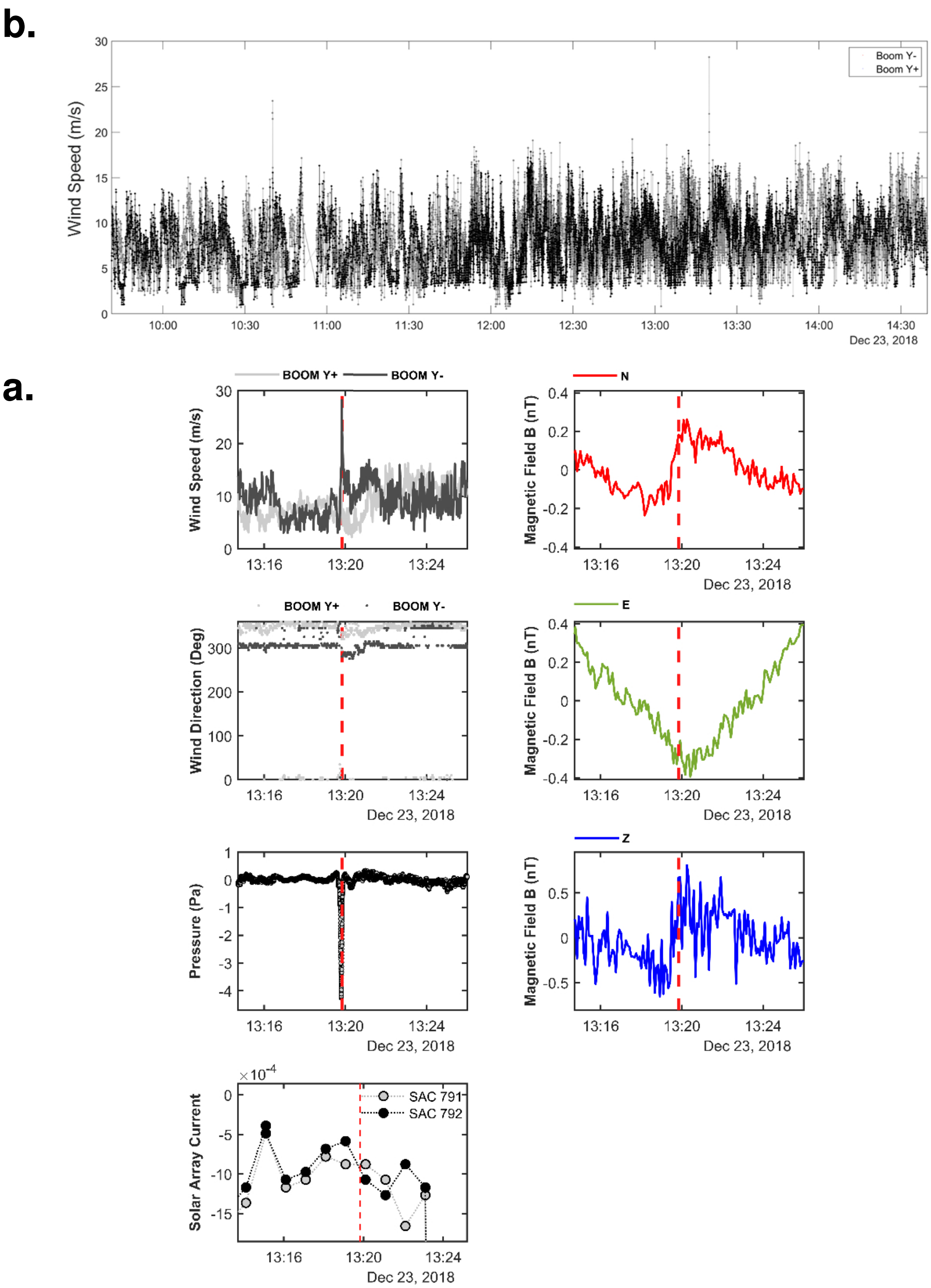

Figure SI5: (a) Wind speed data for the period between the acquisition of the two ICC images that showed motion on the west lander footpad. Two wind peaks are observed, which associate with a 2.9 Pa and 4.1 Pa pressure drop, respectively. (b) Multiple instrument measurements for the most likely candidate vortex that caused footpad changes on sol 26. All instruments show associated excursions correlated to the event, apart from the low-frequency solar array current series (Time axis in UTC).

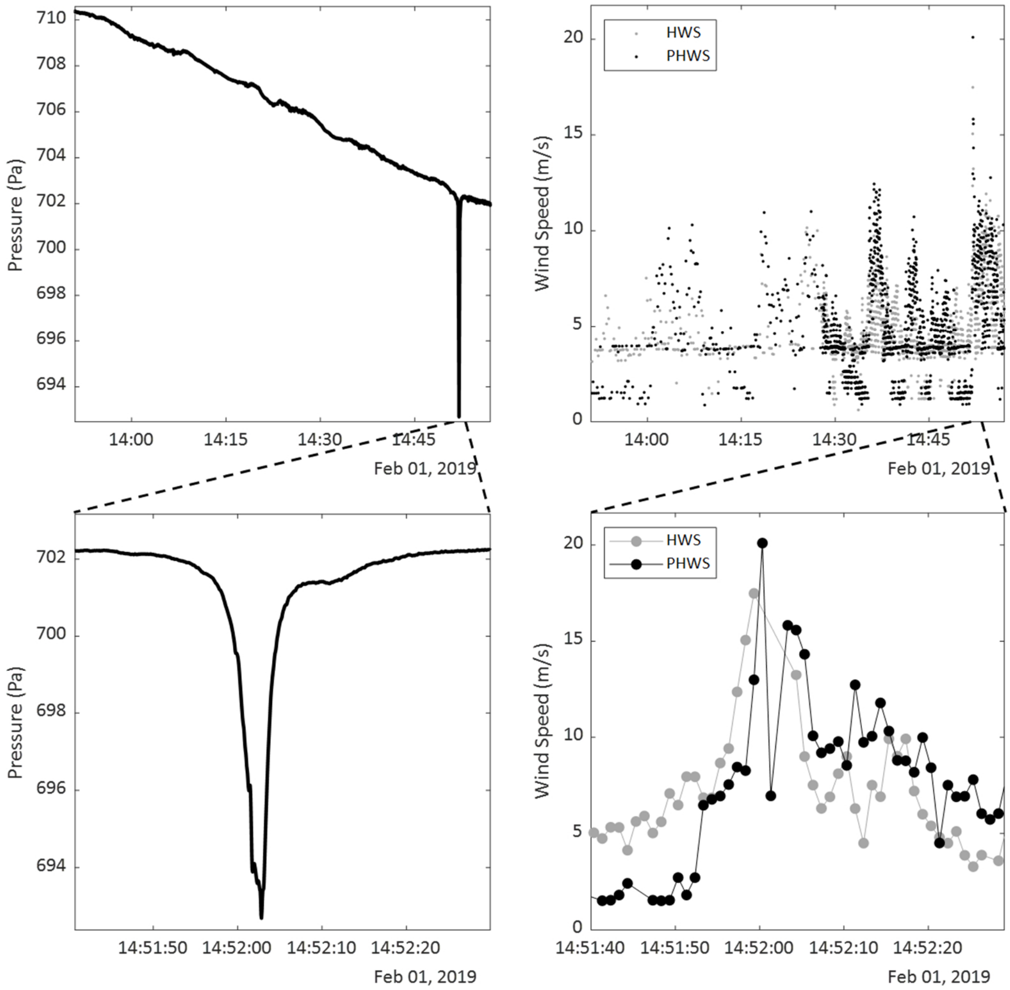

Figure SI6: (Top-Left) Pressure data corresponding to the times between the acquisition of the before and after IDC images shown in the main paper, Fig. 2. The 9 Pa vortex occurred at 14:52 UTC. (Top-Right) Wind data from TWINS, corresponding to the times between the acquisition of the before and after IDC. Note the increase in sampling rate from 14:25 onward. (Bottom) Pressure and wind time-series zoomed at the event over 50 secs, respectively.

SI.10 Sol 65

On sol 65 changes were detected at multiple different locations that were mutually exclusive to the cameras. ICC images taken on sol 65 at 13:48 LMST and sol 66 at 10:05 LMST showed changes on the footpad. These changes are illustrated in Fig. SI6 together with the wind speed and pressure between the times the two images were acquired.

Although grain motion along the deck has been spotted throughout the mission, turbulence on the deck prevents an accurate estimation of the wind speed there. Sol 65 is the only example that imaged particle motion on the WTS and a solar array cleaning event over the 400 sols. These observations were detected between two IDC images during an hourly imaging of the grapple hooked onto the WTS, one sol prior to WTS deployment. Over the interval of one hour, there is only one pressure drop candidate that could be accountable for the observed changes. This is a pressure drop of 9.2 Pa at 2019-02-01 14:52:02 UTC, the largest drop recorded on Mars (Banfield, Spiga 2020) and associated with a wind peak of 20.1 ms^{-1}. The data for the one-hour interval is shown in Fig. SI6. The associated maximum wind speed was 20.1 ms^{-1}, slightly below the fluid threshold of 21 ms^{-1} required for detachment of 100 micron-sized particles (most susceptible to motion) at a z_0 = 1 mm, but still within the resolution of the measurement. The set of solutions is shown in the main text in Fig. 4c.

Missing wind data points during the encounter in the wind record are evident in Fig. SI7, and further investigated in SI13c.

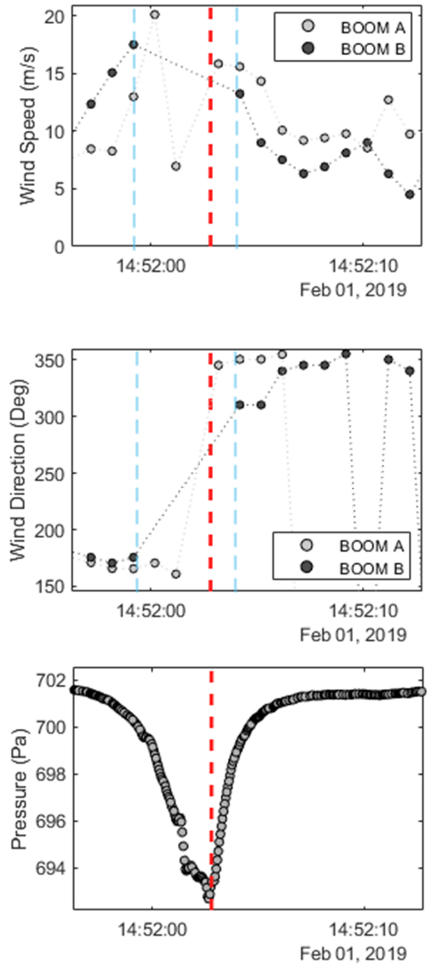

Figure SI7: Sol 65 event wind speed, wind direction and pressure data, respectively. Red dashed line incidates time of maximum pressure drop, while the light-blue dashed lines indicate a period where both booms are missing points due to high perturbations and die saturation from the passing vortex.

SI.11 Sol 235

In addition to the uniform layer of dust that has gradually built up over the course of the mission, distinct aeolian changes were observed on the SEIS tether. Since dust particles gradually get removed, attached or moved along the ICC lens, these dark spots could not be verified until an IDC image was taken on Sol 257.

These spots were identified as areas of localized dust removal from the tether, which revealed its original surface. Later sols reveal these spots were gradually re-covered by dust deposits, thus confirming the hypothesis. This localized removal splashed onto the tether from an unknown trajectory. This is supported by the orientation of all three spots along the tether, with faint tails of dust removed seen on the right side of the largest spot and a horizontal one above (see Fig. 2 in main text and supporting online movie).

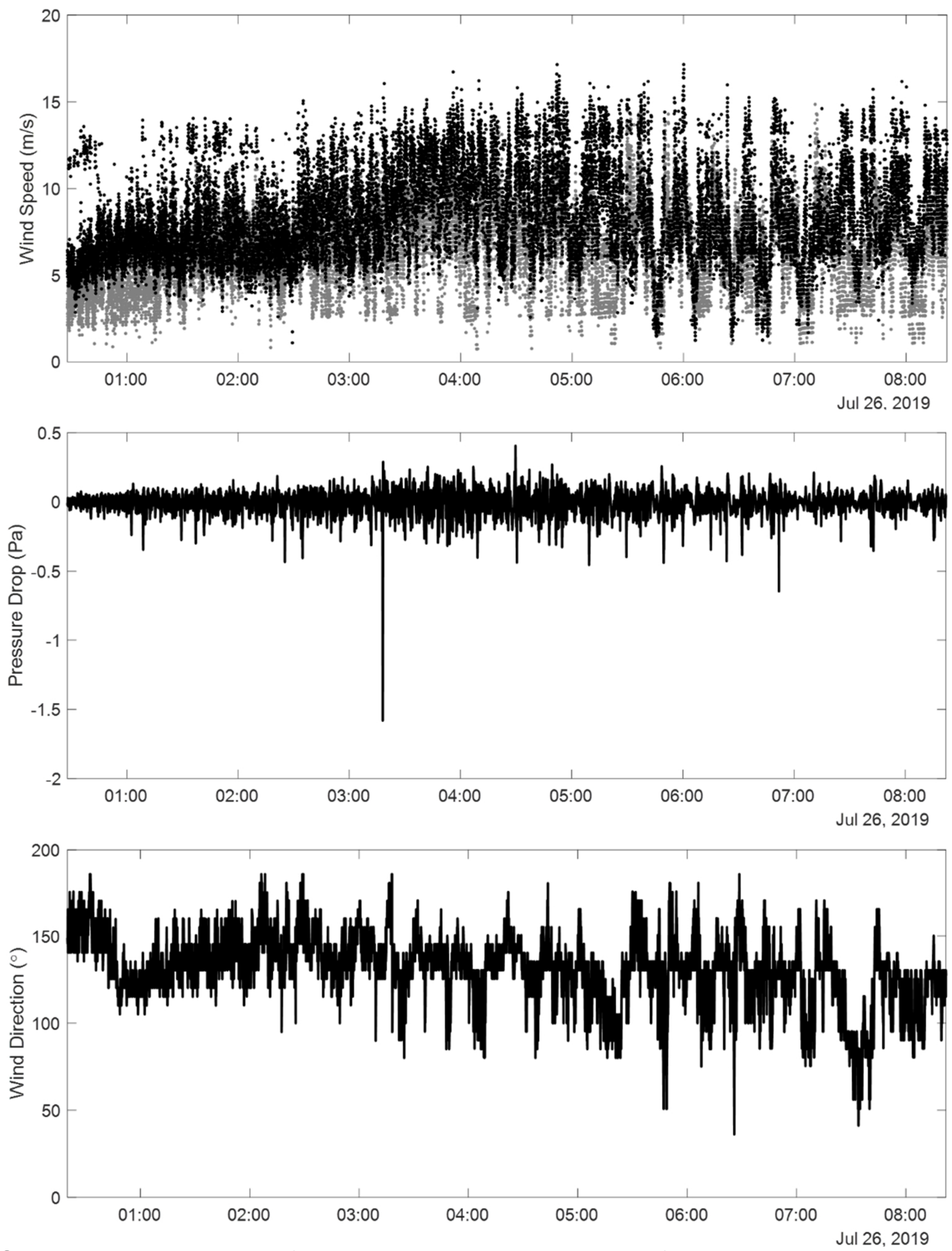

Figure SI8: (Top) Wind speed data for Boom Y- and Y+ over the period for which spots on the tether appeared, believed to be due to localized dust removal, likely from impacts (middle) pressure with a moving mean removed over the same period (bottom) wind direction over the period, indicating a mean ambient wind direction of 140 degrees

SI.12 Sol 364

The S364 shows a peak wind speed of 31.5 ms^{-1}, the maximum recorded over the first 400 sols of operations at InSight. The peak wind speed was associated with a pressure drop at 13:07 LMST on S364 and is characterized by a slightly asymmetrical double dip, likely due to a cycloidal path or a two-core vortex (Lorenz et al. 2016). In contrast to sol 384, this event does not have wind missing data, suggesting that die saturation did not occur. The data suggests that a minimum wind speed of 17 ms^{-1} persisted for at least 40 seconds and possibly longer. While the peak speed may have initiated motion, associated turbulence wind could have driven this further. The changes are illustrated in which the general direction of motion is not consistent. The chaotic trajectory of very small grains could be due to the twist induced by a dust devil, which may serve as indirect evidence of vortex rather than regional wind motion.

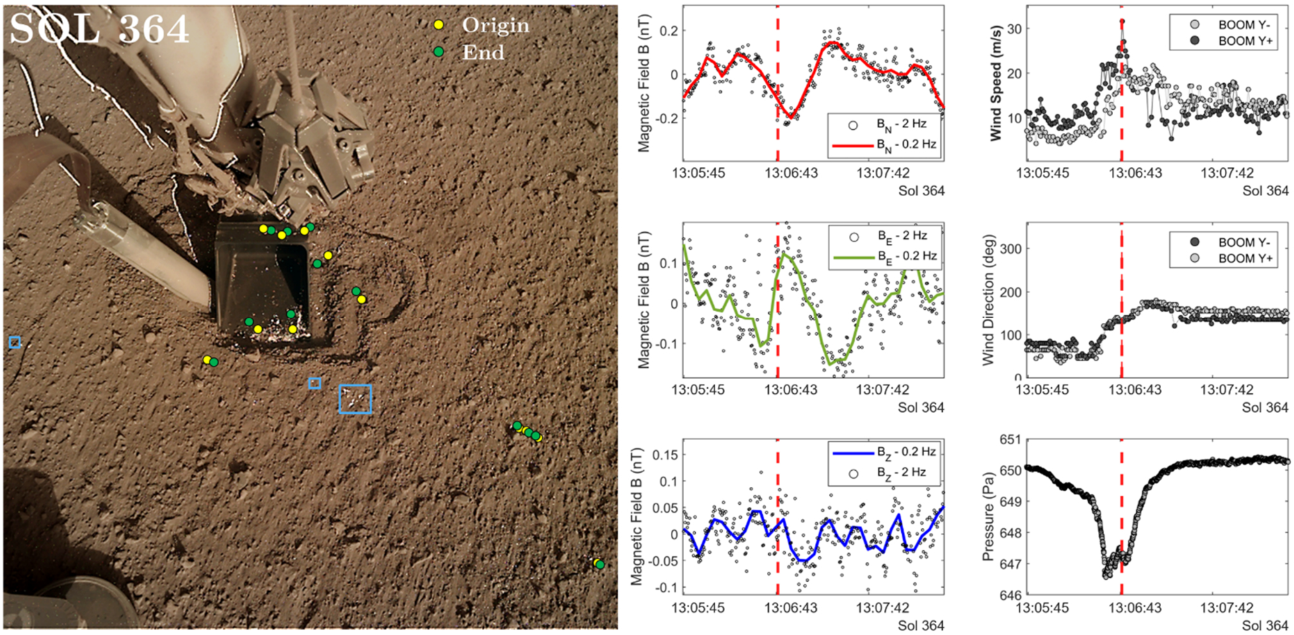

Figure SI9: (Left) Sol 364 aeolian changes. Yellow points indicate the origin and green points indicate the final locations for the most robust grain motion identified. (Middle) Magnetic field data, for B_X, B_Y and B_Z respectively. (Right) Wind speed, wind direction and pressure, respectively

Sol 362_364 grain displacement

image 1 D000M0362_628676418CPG_F0000_0250M1_16h16

image 2 D000M0364_628853969CPG_F0000_0250M116h16

#grain WTS	diameter (mm)
1	2.00
2	1.50
3	1.50
4	2.00
5	1.50

Table SI4: Measurements of the largest particles creeping on sol 364, shown at the right area of Fig. SI9

SI.13 Sol 385

In Fig. SI8, we show how the sol 385 event could be time-constrained between 12:00 LMST and 16:00 LMST. This was achieved by comparing similar illumination images between late afternoon IDC images on sol 383 vs 385 and noon IDC images on sol 385 vs 386. The process is illustrated in Fig. SI7. Particles in motion measured shown and listed in Fig. SI14.

a. Atmospheric modelling

A vortex such as a dust devil yields characteristic histories of pressure and wind as it passes a fixed station. As discussed in Ryan and Lucich (1983) and Lorenz (2016), the wind direction and speed history can be modeled by the superposition of a circumferential vortical flow on the uniform background wind which is assumed to advect the vortex system.

In the case of a diametric encounter (with zero miss distance) the wind speed has a double peak (where the strongest winds at the 'wall' add in quadrature to the background). If a clockwise vortex passes to the east of the station, the circumferential wind reinforces the background, and a wind peak is seen; this geometry and its mirror image may be termed 'additive' encounters. On the other hand, a clockwise vortex passing to the west results in a wind drop, because the circumferential wind opposes the background in a 'contraflow' encounter.

The Sol 385 encounter is in the former category, with the wind speed being enhanced from 12 ms^{-1} to 30 ms^{-1}. There is no evidence of a double peak – either the encounter was not diametric, or the encounter was so rapid that the double peak was not resolved: given that the ambient wind was 12 ms^{-1}, this latter scenario would not be surprising since the wind data are only recorded at 1 sample per second, thus in order to resolve separate twin peaks the diameter would have to be larger than 24 m, which is unusually large. The pressure drop measured is ~6 Pa, thus the core pressure drop ΔP_0 must be at least this large. Assuming cyclostrophic balance, the peak circumferential wind must therefore be at least ~ $(\Delta P_0 /\rho)$^0.5, where ρ is the atmospheric density. Adopting ρ = 0.02 kg/m^3 (Banfield & Spiga, 2020) as a typical value we find the tangential wind V_T > 17 ms^{-1}. The sum of this value and the background wind yields the maximum wind in the system, > 29 ms^{-1}, consistent with the peak observed wind.

The pressure drop measured is 6 Pa, thus the core pressure drop ΔP_0 must be at least this large. Assuming cyclostrophic balance, the peak circumferential wind must therefore be at least ~$(\Delta P_0/\rho)$^0.5. Adopting ρ = 0.02 kgm^{-3} as a typical value we find the tangential wind > 17 ms^{-1}. The sum of this value and the ambient wind yields the maximum wind in the system, > 29 ms^{-1}, consistent with the peak observed wind. These parameters imply a vortex diameter of 10 m or less passing less than one diameter from the lander. All these parameters are consistent with a small (10m or smaller) dust devil making a close encounter, with a miss distance of one diameter or less, and would imply that the maximum wind in the system was not much more than the maximum that was observed by the lander. If we adopt the proposition that the track seen in the ICC image from Fig. 3 (main text) corresponds to this event, then it passed to the west of the lander and to yield the observed winds it must have been rotating counterclockwise.

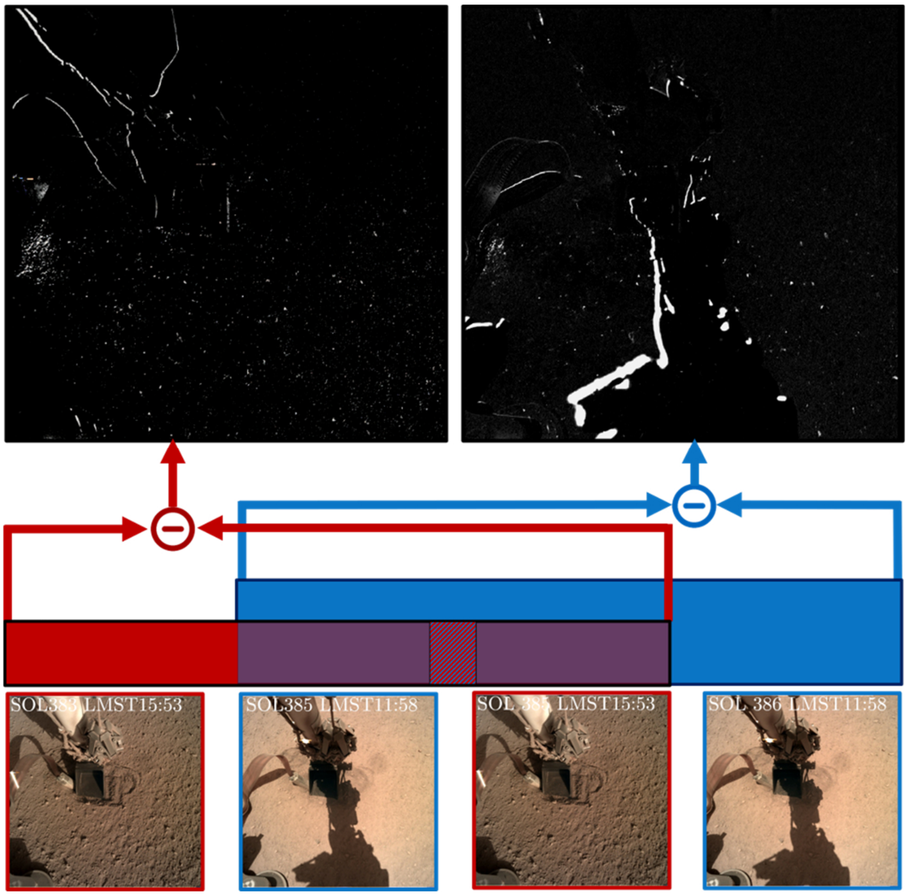

Figure SI10: Sol 385 aeolian changes. The noon and later afternoon images allow us to constrain the event between sol 385 LMST 11:58 and 15:55 (overlapping shadowed area). Top row shows the differenced result of these images. Note the outline on the arm and tether, which demonstrate slight shifts in the illumination conditions.

b. Seismic modelling

The selection of the passing vortex can be validated using the ground acceleration sensed by the seismometers. The model fit (Murdoch et al., 2020) suggests a DD trajectory consistent with the track observed in the ICC image difference (Fig. SI11) and from the HiRISE orbital imagery with the dominant wind direction of approximately 130° from North measured by the TWINS. Therefore, this validates the selection of this pressure drop in the time-lapsed interval as the one that caused the aeolian changes observed.

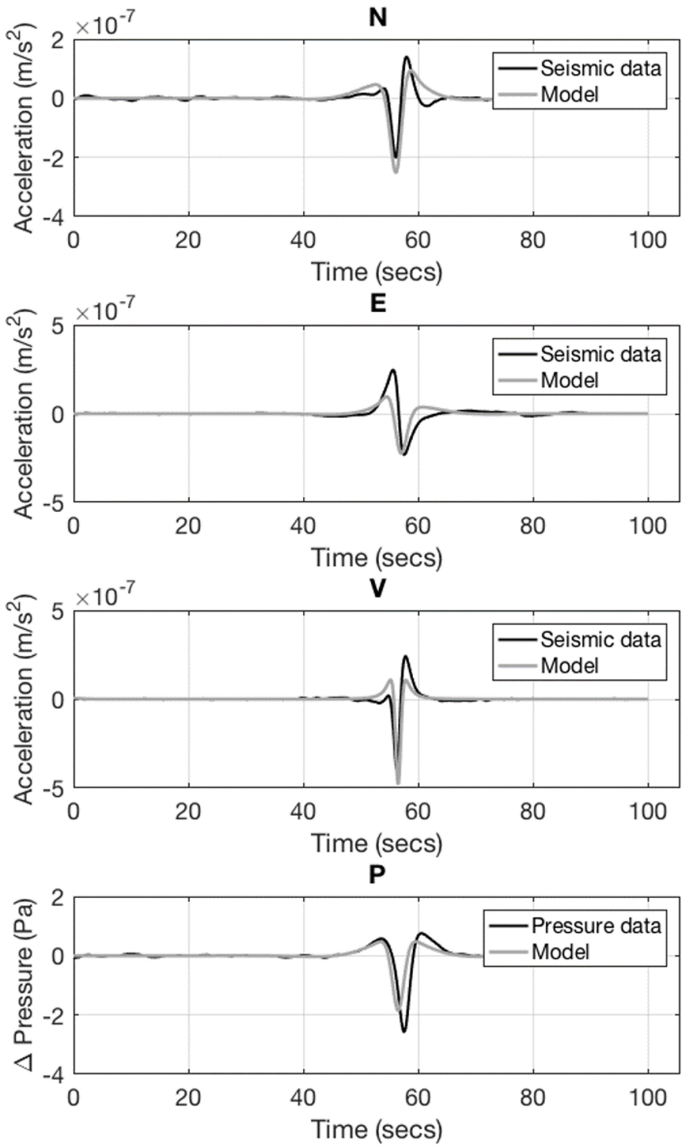

Figure SI11: Model fitting of the sol 385 vortex and its trajectory using the ground acceleration from SEIS and the pressure data. The pressure data and Very Broad Band (VBB) seismometer's data for each of the East, North and Vertical components in black, and the model's in grey, have been filtered in the 0.05 - 0.3 Hz bandwidth. The fit suggests a DD trajectory consistent with the track in the ICC image and the dominant wind direction of approximately 130°, and therefore further validates the selection of this pressure drop as the one that has caused the aeolian changes.

c. Missing wind data

The passing vortex was observed as a transient pressure drop of approximately 7 seconds in duration, suggesting the aeolian changes induced were very short-lived, not accounting for hysteresis. TWINS, measuring at 1 sample per second, was not able to retrieve reliable measurements, marked as

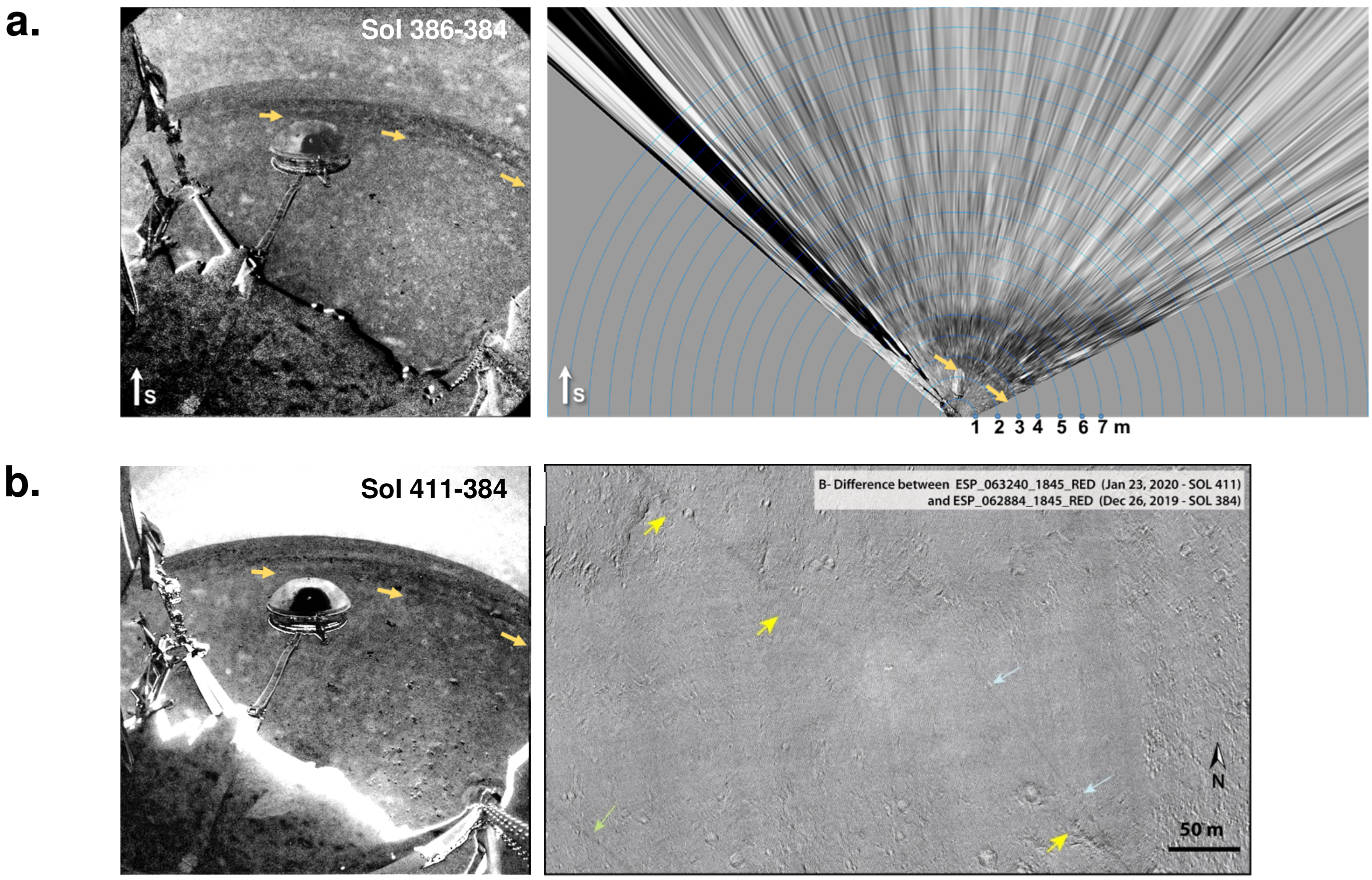

Figure SI12: (a) Map-projection of the Sol 385 DD track, with contours of distance in blue from the ICC origin at each meter from R = 2 to 10 m. From the camera, the near side of the track was 2.5 m away, and the far side was ~7 m away. The track is estimated to have approached SEIS within ~1 m. ICC map-projection is more accurate the nearer it is to the fish lens. We therefore take the trajectory of the inner half of the track, approximating a source direction of 120-130 degrees from the north, in agreement with the seismic and atmospheric modelling of the event (b) ICC image differencing for images spanning the same period as the orbital images. The track still appears in the ICC image and therefore provides proof that track erasure did not occur over the orbital image differencing period from sol 384 to sol 411, pointed by the yellow arrows. The green and blue arrows in the orbital image differencing indicate two further DD tracks identified as forming between sol 384 to sol 411.

spurious points, during the closest encounter with the vortex due to high perturbations and die saturation. The missing data points are illustrated in Fig. S9, which can be seen as missing markers at a consistent sampling rate on the dotted line. Since measurements over at least two seconds of the maximum ΔP during a 7-second transience were not derivable from the TWINS data on S385 under very high vorticity conditions resulting in saturation (Fig. SI12). Therefore, wind speeds are likely to be substantially higher than 30 ms^{-1}. This might explain the discrepancy between the significantly stronger motion observed on sol 385 at a lower wind speed than the stronger wind on sol 364, which in contrast induced a very limited motion

d. HiRISE orbital image differencing of S384-S413

The regular acquisition of HiRISE images (McEwen et al., 2007) allow us to monitor the surface changes related to the atmospheric activity around the InSight lander, such as dust-devil tracks formed by passing convective vortices (Banerdt et al., 2020; Banfield et al., 2020; Perrin et al., 2020). On the new image acquired on sol 411 (Jan 23, 2019; ESP_063240_1845_RED), several tracks were detected around the lander (Fig.4a). The closest one (yellow arrows) is situated SW of the lander, trending N130±2°E, at a distance of ~5m from SEIS at its closest approach. The track is at least 5-6 m wide and its trace is fainted as it comes close to the lander, due to the lack of dust that has been removed from the ground during landing. This track is consistent to the characteristics of the S385 DD track, and since it falls within the period of the two orbital image acquisition, it is very likely the same track.

.

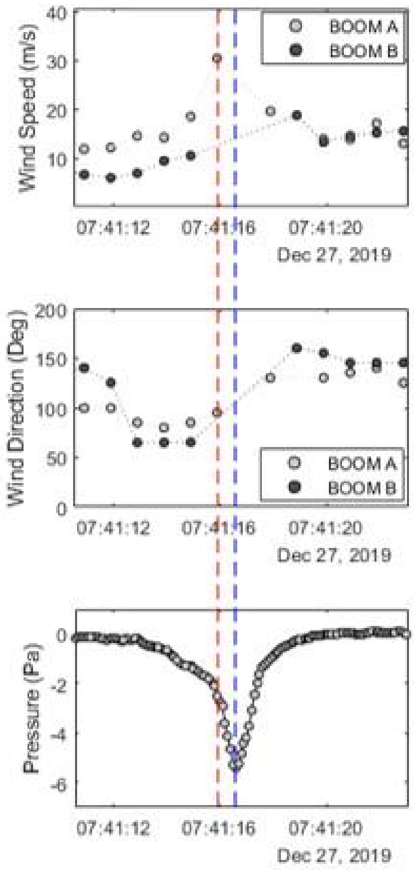

Figure SI13: This figure emphasises the missing wind data retrieval due to increased perturbations on the lander from the vortex encounter on S385. The steepest gradient in the pressure drop is indicated by the red dashed line, which aligns to the maximum measured wind peak. From thereon, both sensors have missing data points, seen as a non-constant interval. The time of maximum pressure drop, and therefore closest encounter, is shown by the blue dashed line, at an interval where both TWINS booms are missing data points.

Particle Number	Diameter (cm)
18	0.3
1	0.285
29	0.285
25	0.271
17	0.261
27	0.258
20	0.255
21	0.251
34	0.248
16	0.246
3	0.235
4	0.233
23	0.22
11	0.216
26	0.212
31	0.211
7	0.199
10	0.196
28	0.189
13	0.182
14	0.177
5	0.176
9	0.176
2	0.169
12	0.166
6	0.164
24	0.163
8	0.157
22	0.145
30	0.145
15	0.141
19	0.14
33	0.137
32	0.124

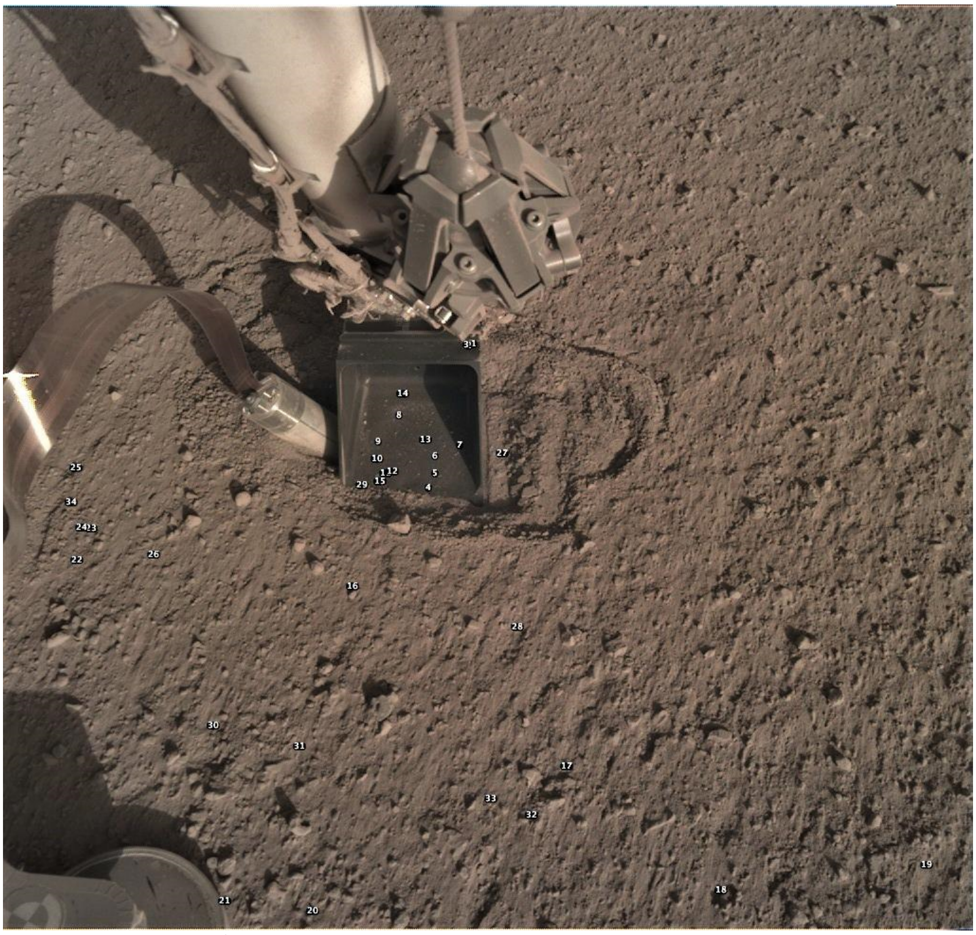

Figure SI14: Measurements for the most robustly identified and resolvable particle motion on sol 385, as numbered by the accompanied image.

SI.14 Orbital image investigation for aeolian changes

We investigated HiRISE orbital images between periods during which changes were observed by the lander: S14 and S16, and S357, S384 and S413. We see what could potentially be evidence for movement of sediments inside craters and blowing sediments covering up some bright albedo features or small rocks on the surface. However, these observations could be explained by differences in lighting conditions, parallax, or noise (although we note that these changes are not obs erved in all craters and similar and adjacent features on the surface). We also explored a few dust devil tracks near InSight that appeared from dust devil activity during the time period between each HiRISE image pair. Again, we observe some potential evidence of movement of sediments, but nothing yet conclusive at this scale, with a resolution of 25 cm/pixel.

SI.15 Sand Grains Near the HP3 Mole

The robotic arm may have accumulated, apart from dust, numerous sand grains as well. These became evident when the arm was pinned on the HP3 mole. Hammering-induced vibrations could have caused these grains to detach and drop on the surface. It is unclear whether the sand grains were placed on the arm during landing, but it is a curiosity how they could remain attached over 300 sols of repeated IDA use. Another scenario would have these grains propel and bounce off the scoop during the hammering vibrations.

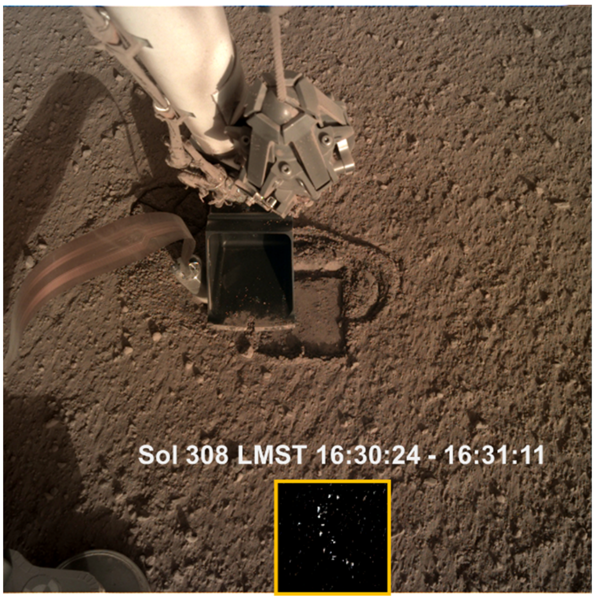

Figure SI15: HP3 hammering during sol 308. The golden inset depicts the result of image differencing which shows new particles emerging in the scene between the onset of hammering and 40 seconds later. These have likely bounced off the scoop or fallen off the robotic arm.

SI.16 Maximum wind shear

Given the diameter of the smallest and largest particles that did not move between a pair of images, the maximum wind shear that occurred between that pair of images can be estimated using Shao & Lu (2000):

$$u^*_{\mathrm{max}} = A_{\mathrm{N}} \sqrt{\frac{\rho_{\mathrm{p}} - \rho_{\mathrm{a}}}{\rho_{\mathrm{a}}} g d_{\mathrm{p}} + \frac{\gamma}{\rho_{\mathrm{a}} d_{\mathrm{p}}}}, \tag{2}$$

where A_N is a constant ≈ 0.0123, $\rho_p \approx 2900$ kgm^{-3} the density of the particles, $\rho_a \approx 0.02$ kgm^{-3} the density of the atmosphere, $g \approx 3.71$ ms^{-2} the acceleration due to gravity, d_p the diameter of the smallest or largest particle that did not move between images, and $\gamma \approx 3$ x10^{-4} kgs^{-2} an empirical constant describing the strength of the interparticle forces. The the complete set of solutions that meet the u^*_t threshold conditions for incipient grain motion based on the peak wind speed of 28.2 ms^{-1} on Sol 26 can thus be estimated and is shown in Fig. S16. A comparison of Shao and Lu (2000) to Merrison's et al., (2007) drag-induced roll model, is shown in Fig. S17. The latter model indicates that u^*_t needs only be sufficiently smaller to entrain mm-sized grains, with the two models diverging at ~300 microns.

The surface roughness z_0 can also be estimated assuming a logarithmic wind profile:

$$z_0 = z \exp\left(-\frac{\kappa u_x}{u^*_{\mathrm{max}}}\right) \tag{3}$$

where z is the height at which the horizontal wind speed is measured, κ = 0.4 the von Kármán constant, and u_x the horizontal wind speed.

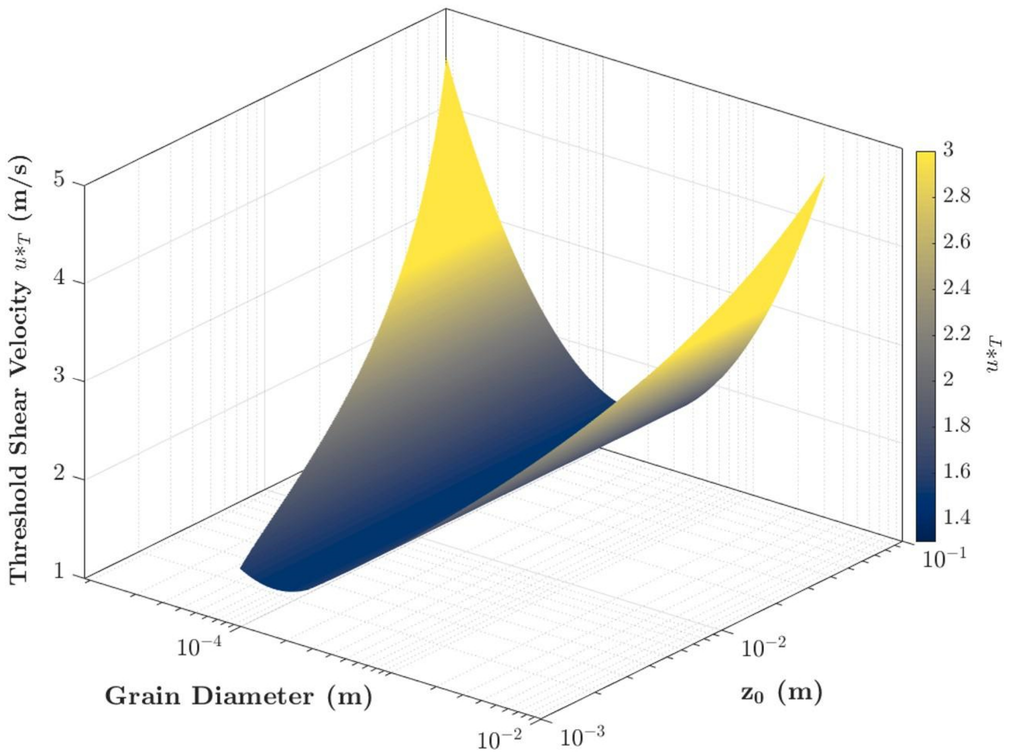

Figure S16: This surface represents the complete set of solutions that meet the u_{*t} threshold conditions for incipient grain motion based on the peak wind speed of 28.2 ms^{-1} on Sol 26. The set varies between a range of particle sizes and z_0 values. The figure in the main text Fig. 4d attempts to restrict these two unknowns by investigating the maximum and minimum wind speeds which induced surface detachment. The unknown critical parameters stem from: 1) Since z_0 is uncertain and varies substantially across areas at InSight and 2) The size range of the particles, for example the patch of dust on the west footpad is unknown because the image resolution is not sufficient 3) Unreliable wind speed measurements during a vortex's passage .

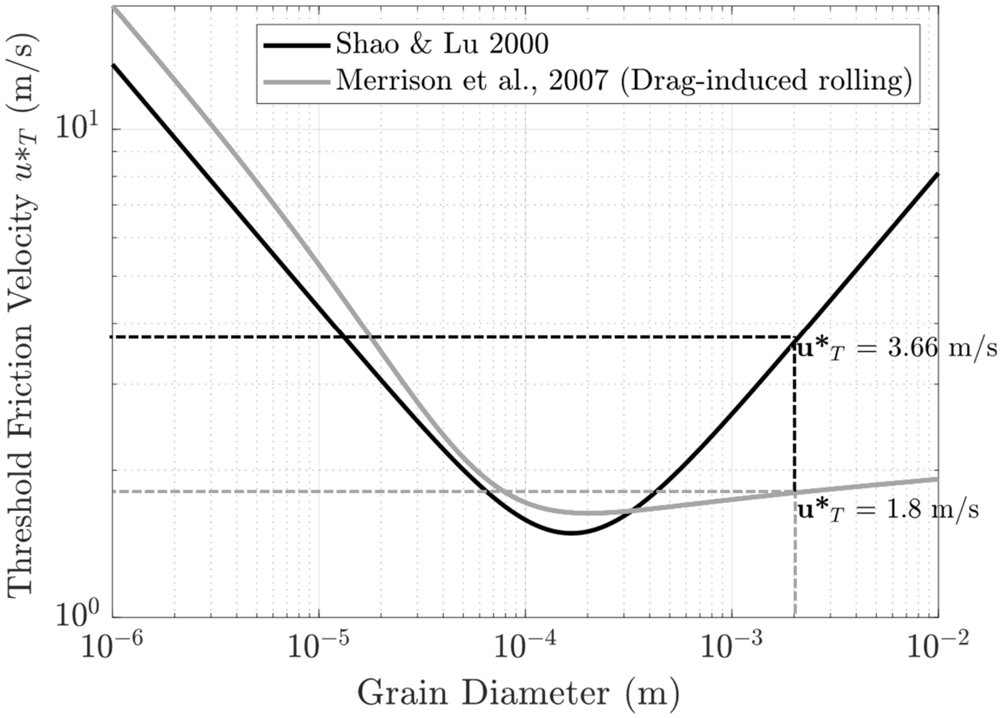

Figure S17: Two different models that quantify the threshold friction velocity $u*_T$ required for particle entrainment by the wind, by Shao and Lu (2000), and Merrison et al., 2007. Of specific interest are the 2 *mm* grains, which are seen to be in traction, likely due to drag-induced rolling, on Sol 364 and 385 for wind speed of 31.5 ms^{-1} and 30 ms^{-1}, respectively. In contrast, the 2 *mm* grains on the west footpad were not entrained at any time between Sol 10 - 106, while the dusty layer was removed at a maximum observed wind speed of 28.2 ms^{-1}.

SI.17 Seismic data exploitation

Although beyond the scope of this work, particles that impact the tether could potentially be detected by the seismometers. Since the tether is connected to SEIS and is sensitive to electric fields, charged grains could induce an electric-field noise detectable by SEIS (Clinton et al, 2017). Approaches include the exploitation of the high-cadence seismometers as wind sensors via the co-modulation framework by (Charalambous, C., et al., this issue). Such a framework can estimate the wind and pressure directly from the energy of regolith deformations due to wind-induced lander vibrations and further predict signals that did not originate from direct environmental noise, such as saltator impacts on the tether. These together can also potentially improve the meteorological data.

SI.18 Shadow spots by the WTS

Occasionally, dark spots appear in the ICC's FOV, sometimes associated with new DD tracks. A DD passage from S232-S230 may have caused albedo changes from entrainment of localized dust layers appearing as dark ellipsoids. An example is shown by the black arrow in Fig. SI15a. S385 shows similar dark spots on protruding rocks, confirmed by the IDC, suggesting strong passing vortices could entrain local dust deposits. However, without IDC confirmation, these spots deserve caution as dust settlement on the ICC lens can produce similar optical artefacts (Fig. SI15b).

Fig. SI15b demonstrates a pair of image differencing where these spots appear nearby the WTS. Notice how one of the spots appears along the WTS skirt, and therefore these cannot be attributed to surface changes, but possibly wind-blown dust particles on the ICC lens.

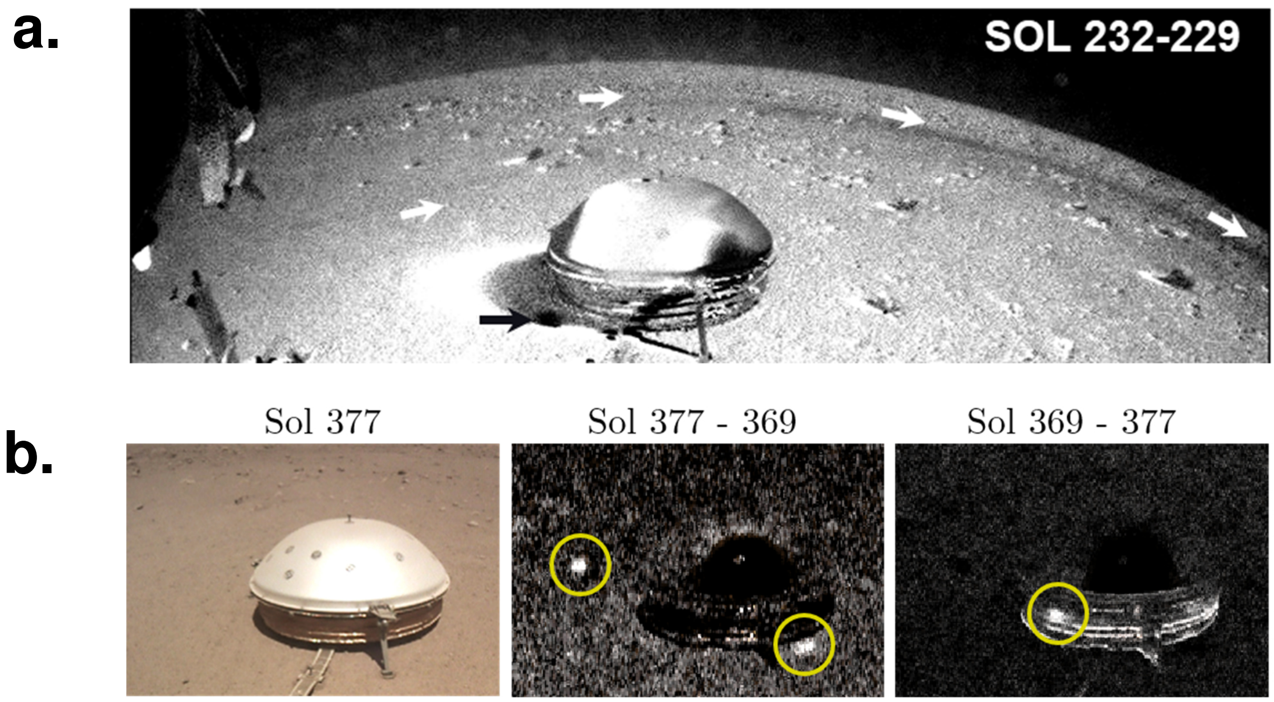

Figure SI18: (a) Image differencing of Sol 232-229, indicating the DD track emerging and a dark localized spot by the WTS, as a potential surface change. Removal of dust particles on lens are indicated as faint dark spots, therefore a dark spot indicates a surface change, indicative of dust removal. (b) Image differencing via two ways by subtracting sols as 377–369 and 369–377. The circled white areas by the WTS in the 377–369 difference indicate the disappearance of dark spots on sol 377. The circled white area in the 369 – 377 difference indicates the appearance of a dark spot on the WTS skirt on sol 377. In the online GIF movie, the leftmost spot is seen shifting downwards between Sol 369 and 377 and can be attributed to a dust particle moving on the ICC lens.

SI.19 Incorporating deployed instruments as roughness elements within InSight's workspace

Incorporating the deployed instruments of SEIS and HP3 in the workspace as roughness elements, raises the total fractional area covered by the rocks within the workspace to over 10%, a percentage equal to that between Viking Lander 2 and Mars Pathfinder. These two sites have had their aerodynamic surface roughness lengths z_0 estimated at z_0 = 1 cm and 3 cm, respectively. Therefore, this provides an approximation for the local z_0 for InSight's workspace to these values. Fig SI16 shows the cumulative fractional area rock distributions for previous missions, and how those compare to InSight workspace by taking account the rocks only in comparison by incorporating the deployed instruments of SEIS/WTS and HP3 as roughness elements. This result indicates highly heterogeneous surface roughness values within Homestead hollow. This is due to the highly populated area by the lander, a smoother area of the hollow to the east and a more densely rock distribution transition to the west and beyond the hollow (Charalambous et al., 2019). Further roughening is induced by the SEIS tether, the HP3 tether, disturbed areas by the HP3 mole, disturbed/excavated area beneath the lander by the retrorockets, the lander itself, and the positioning of the arm or scoop, while pinned to the surface.

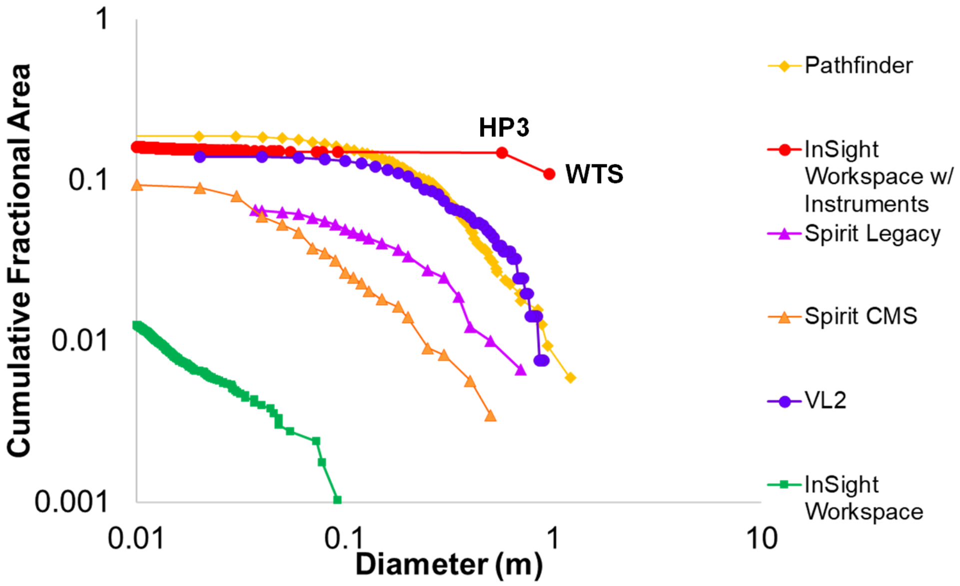

Figure SI19: Cumulative fractional areas of rock distribution of previous Mars landed missions in comparison to InSight's workspace of just rocks, against one (**red**) incorporating deployed instruments (WTS and HP3) as roughness elements.

.

References

Bagnold, R. (1941). The physics of blown sand and desert dunes.

Baker, M.M., Lapotre, M.G., Minitti, M.E., Newman, C.E., Sullivan, R., Weitz, C.M., Rubin, D.M., Vasavada, A.R., Bridges, N.T. and Lewis, K.W., 2018. The Bagnold Dunes in southern summer: Active sediment transport on Mars observed by the Curiosity rover. Geophysical Research Letters, 45(17), pp.8853-8863

Baker, M.M., Newman, C., Charalambous, C., Golombek, M., Spiga, A., Banfield, D., Lemmon, M., Banks, M., Garvin, J., Grant, J., Lewis, K., Ansan, V., Warner, N., Weitz, C., Wilson., S., The modern aeolian environment at Homestead hollow, Mars, *JGR Planets, this issue*

Baker, M.M., Lapotre, M.G., Minitti, M.E., Newman, C.E., Sullivan, R., Weitz, C.M., Rubin, D.M., Vasavada, A.R., Bridges, N.T. and Lewis, K.W., 2018. The Bagnold Dunes in southern summer: Active sediment transport on Mars observed by the Curiosity rover. Geophysical Research Letters, 45(17), pp.8853-8863

Balme, M. R., & Greeley, R. (2006). Dust devils on Earth and Mars. *Reviews of Geophysics*, *44*, 3003-+. doi: 10.1029/2005RG000188

Banerdt, W. B., co authors, & the InSight team. (n.d.). Nature Geoscience (this issue).

Banfield, D., Spiga, A., & co authors. (2020). *The atmosphere of mars as observed by insight.* Revised version submitted to Nature Geoscience.

Bridges, N. T., Ayoub, F., Avouac, J. P., Leprince, S., Lucas, A., & Mattson, S. (2012). Earth-like sand fluxes on Mars. *Nature*, *485*(7398), 339-342.

Clinton, J. F., Giardini, D., Lognonné, P., Banerdt, B., van Driel, M., Drilleau, M., ... & Golombek, M. (2017). Preparing for InSight: An invitation to participate in a blind test for Martian seismicity. *Seismological Research Letters*, *88*(5), 1290-1302.

Eden, H. F., & Vonnegut, B. (1973). Electrical breakdown caused by dust motion in low-pressure atmospheres: Considerations for Mars. *Science*, *180*(4089), 962-963.

Farrell, W. M. Electric and magnetic signatures of dust devils from the 2000–2001 MATADOR desert tests. J. Geophys. Res. 109,E03004 (2004).

Geissler, P. E., Sullivan, R., Golombek, M., Johnson, J. R., Herkenhoff, K., Bridges, N., Vaughan, A., Maki, J., Parker, T., and Bell, J., 2010, Gone with the Wind: Eolian erasure of the Mars rover tracks, Journal of Geophysical Research, Planets, v. 115, E00F11, doi:10.1029/2010JE003674.

Gierasch, P. J., & Goody, R. M. (1972). The effect of dust on the temperature of the Martian atmosphere. *Journal of the Atmospheric Sciences*, *29*(2), 400-402.

Golombek, M., co authors, & the InSight team. (2020). *Geology of the InSight landing site, Mars.* Nature Communications (in press).

Golombek, M., Huertas, A., Kipp, D., & Calef, F. (2012). Detection and characterization of rocks and rock size-frequency distributions at the final four mars science laboratory landing sites. *International Journal of Mars Science and Exploration*, *7*, 1–22.

Golombek, M., Kipp, D., Warner, N., Daubar, I. J., Fergason, R., Kirk, R. L., ... Banerdt, W. B. (2017). Selection of the InSight Landing Site. *Space Science Reviews*, *211*, 5-95. doi: 10.1007/s11214-016-0321-9

Golombek, M., Grott, M., Kargl, G., Andrade, J., Marshall, J., Warner, N., ... & Lichtenheldt, R. (2018). Geology and physical properties investigations by the InSight lander. *Space Science Reviews*, *214*(5), 84.

Greeley, R. (2002). Saltation impact as a means for raising dust on Mars. *Planetary and Space Science*, *50*, 151-155. doi: 10.1016/S0032-0633(01)00127-1

Greeley, R., Kuzmin, R. O., Rafkin, S. C. R., Michaels, T. I., & Haberle, R. (2003). Wind-related features in Gusev crater, Mars. *Journal of Geophysical Research (Planets)*, *108*(E12), 8077. doi: 10.1029/2002JE002006

Greeley, R., Waller, D. A., Cabrol, N. A., Landis, G. A., Lemmon, M. T., Neakrase, L. D., ... & Whelley, P. L. (2010). Gusev Crater, Mars: Observations of three dust devil seasons. *Journal of Geophysical Research: Planets*, *115*(E7).

Hebrard, E., Listowski, C., Coll, P., Marticorena, B., Bergametti, G., M¨a¨att¨anen, A., ... Forget, F. (2012). An aerodynamic roughness length map derived from extended martian rock abundance data *Journal of Geophysical Research*, *117*(E4), E04008.

Hecht, M. H., McClean, J. B., Pike, W. T., Smith, P. H., Madsen, M. B., Rapp, D., & Team, M. (2017, June). MOXIE, ISRU, and the History of In Situ Studies of the Hazards of Dust in Human Exploration of Mars. In *Dust in the Atmosphere of Mars and Its Impact on Human Exploration* (Vol. 1966).

Hess, S. L., Henry, R. M., Leovy, C. B., Ryan, J. A., & Tillman, J. E. (1977). Meteorological results from the surface of Mars: Viking 1 and 2. *J. Geophys. Res.*, *82*, 4559-4574.

Holstein-Rathlou, C., Gunnlaugsson, H. P., Merrison, J. P., Bean, K. M., Cantor, B. A., Davis, J. A., ... Taylor, P. A. (2010). Winds at the Phoenix landing site. *Journal of Geophysical Research (Planets)*, *115*(12), E00E18. doi: 10.1029/2009JE003411

InSight Mars SEIS Data Service. (2019). SEIS raw data, Insight Mission. IPGP, JPL, CNES, ETHZ, ICL, MPS, ISAE-Supaero, LPG, MFSC. https://doi.org/10.18715/SEIS.INSIGHT.XB_2016Iversen, J. D., & White, B. R. (1982). Saltation threshold on earth, mars and venus. *Sedimentology*, *29*(1), 111–119.

Jackson, T. L. & Farrell, W. M. Electrostatic fields in dust devils: an analog to Mars. IEEE Trans. Geosci. Remote Sens. 44, 2942–2949 (2006).

Kok, J. F., Parteli, E. J. R., Michaels, T. I., & Karam, D. B. (2012, January). The physics of wind-blown sand and dust. *ArXiv e-prints*.

Kurgansky, M. V., Baez, L. & Ovalle, E. M. A simple model of the magnetic emission from a dust devil. J. Geophys. Res. 112, E11008 (2007).,

Lapotre, M., Ewing, R., Lamb, M., Fischer, W., Grotzinger, J., Rubin, D., ... others (2016). Large wind ripples on mars: A record of atmospheric evolution. *Science*, *353*(6294), 55–58.

Lorenz, R.D., 2016. Heuristic estimation of dust devil vortex parameters and trajectories from single-station meteorological observations: Application to InSight at Mars. Icarus, 271, pp.326-337

Lorenz, e. a., R. (2020). Scientific Observations with the InSight Solar Arrays : Dust, Clouds and Eclipses on Mars. *this issue*.

Madeleine, J. B., Forget, F., Millour, E., Montabone, L., & Wolff, M. J. (2011). Revisiting the radiative impact of dust on Mars using the LMD Global Climate Model. *Journal of Geophysical Research: Planets*, *116*(E11).

Maki, J. N., Golombek, M., Deen, R., Abarca, H., Sorice, C., Goodsall, T., ... Banerdt, W. B. (2018, Aug 29). The color cameras on the insight lander. *Space Science Reviews*, *214*(6), 105. Retrieved from https://doi.org/10.1007/ s11214-018-0536-z doi: 10.1007/s11214-018-0536-z

Marticorena, B., Kardous, M., Bergametti, G., Callot, Y., Chazette, P., Khatteli, H., ... others (2006). Surface and aerodynamic roughness in arid and semiarid areas and their relation to radar backscatter coefficient. *Journal of Geophysical Research: Earth Surface*, *111*(F3).

McEwen, A. S., Eliason, E. M., Bergstrom, J. W., Bridges, N. T., Hansen, C. J., Delamere, W. A., et al. (2007). Mars reconnaissance orbiter's high resolution imaging science experiment (HiRISE). *Journal of Geophysical Research E: Planets*, *112*(5), 1–40. https://doi.org/10.1029/2005JE002605

Merrison, J. P., Gunnlaugsson, H. P., Nørnberg, P., Jensen, A. E., & Rasmussen, K. R. (2007). Determination of the wind induced detachment threshold for granular material on mars using wind tunnel simulations. *Icarus*, *191*(2), 568–580.

Newman, C. E., S. R. Lewis, P. L. Read, and F. Forget, Modeling the Martian dust cycle, 1, Representations of dust transport processes, J. Geophys. Res., 107(E12), 5123, doi:10.1029/2002JE001910, 2002.

Newman, C. E., Gómez-Elvira, J., Marin, M., Navarro, S., Torres, J., Richardson, M. I., ... & Vasavada, A. R. (2017). Winds measured by the Rover Environmental Monitoring Station (REMS) during the Mars Science Laboratory (MSL) rover's Bagnold Dunes Campaign and comparison with numerical modeling using MarsWRF. *Icarus*, *291*, 203-231.

Perrin, C., Rodriguez, S., Jacob, A., Lucas, A., Spiga, A., Murdoch, N., et al. (2020). Monitoring of Dust-Devil Tracks Around the InSight Landing Site, Mars, and Comparison with in-situ Atmospheric Data. *Geophysical Research Letters*, *this issue*.

Prandtl, L., & Tietjens, O. G. (1934). *Applied hydro- and aeromechanics*. New-York: Dover Publications, Inc.

Ryan, J.A. and Lucich, R.D., 1983. Possible dust devils, vortices on Mars. Journal of Geophysical Research: Oceans, 88(C15), pp.11005-11011.

Schofield, J. T., Crisp, D., Barnes, J. R., Haberle, R. M., Magalhaes, J. A., Murphy, J. R., ... Wilson, G. (1997). The Mars Pathfinder Atmospheric Structure Investigation/Meteorology (ASI/MET) experiment. *Science*, *278*, 1752-1757.

Shao, Y., & Lu, H. (2000). A simple expression for wind erosion threshold friction velocity. *Journal of Geophysical Research: Atmospheres*, *105*(D17), 22437–22443.

Sullivan, R., & Kok, J. (2017). Aeolian saltation on mars at low wind speeds. *Journal of Geophysical Research: Planets*, *122*(10), 2111–2143.

Sutton, J. L., Leovy, C. B., & Tillman, J. E. (1978). Diurnal variations of the Martian surface layer meteorological parameters during the first 45 sols at two Viking lander sites. *J. Atmos. Sci.*, *35*, 2346-2355.

Wurm, G., Teiser, J., & Reiss, D. (2008). Greenhouse and thermophoretic effects in dust layers: The missing link for lifting of dust on mars. *Geophysical Research Letters*, *35*(10).